PHYSICAL REVIEW E **94**, 063115 (2016)

Effective slip for flow in a rotating channel bounded by stick-slip walls

Chiu-On Ng[*]
Department of Mechanical Engineering, The University of Hong Kong, Pokfulam Road, Hong Kong

(Received 23 July 2016; revised manuscript received 22 November 2016; published 28 December 2016)

This paper aims to look into how system rotation may modify the role played by boundary slip in controlling flow through a rotating channel bounded by stick-slip walls. A semianalytical model is developed for pressure-driven flow in a slit channel that rotates about an axis perpendicular to its walls, which are superhydrophobic surfaces patterned with periodic alternating no-shear and no-slip stripes. The cases where the flow is driven by a pressure gradient parallel or normal to the stripes are considered. The effects of the no-shear area fraction on the velocities and effective slip lengths for the primary and secondary flows are investigated as functions of the rotation rate and the channel height. It is mathematically proved that the secondary flow rate is exactly the same in the two cases, irrespective of whether the primary flow is parallel or normal to the wall stripes. For any rotation speed, there is an optimal value of the no-shear area fraction at which the primary flow rate is maximum. This is a consequence of two competing effects: the no-shear part of the wall may serve to reduce the wall resistance, thereby enhancing the flow especially at low rotation, but it also weakens the formation of the near-wall Ekman layer, which is responsible for pumping the flow especially at high rotation. Wall slip in a rotating environment is to affect flow in the Ekman layer, but not flow in the geostrophic core.

DOI: 10.1103/PhysRevE.94.063115

I. INTRODUCTION

Much work has been done in the past decade on achieving drag reduction in wall-bounded low-Reynolds-number flow by means of a microtextured surface over which slip may occur. Hydrodynamic slip refers to the phenomenon in which the traditional no-slip boundary condition is not observed, but a fluid may slip past the surface of an object. Such slip is usually an apparent phenomenon, occurring on a chemically coated hydrophobic surface, an interface between a porous medium and clear fluid, a lubricant-impregnated surface, a superhydrophobic surface, and so on. In particular, a superhydrophobic surface is a microengineered surface, which is so fabricated that the microfeatures in the form of ribs, pillars, or holes may trap a low-viscosity fluid, usually a gas, in the minute cavities. In the Cassie state, where a liquid does not penetrate the gas-filled cavities, the flow of a liquid will be effectively lubricated by the gas phase trapped in the microfeatures. Nizkaya *et al.* [1] recently proposed a gas-cushion model for superhydrophobic textures.

Slip is usually measured by a quantity known as the slip length, which can be interpreted as the distance into the envelope of a surface where the velocity profile would extrapolate to a zero velocity. If Navier's slip condition [2] is followed, the slip length is also equal in magnitude to the slip velocity divided by the near-wall velocity gradient. A slip length can range from zero to infinity, corresponding to no-slip and no-shear (or perfect-slip) surfaces, respectively.

Owing to the composite nature of a microtextured surface, the local slip length may vary widely between zero and infinity over a short distance, and analysis will be difficult if such spatial variations on the microscale are fully accounted for. In practice, it suffices if the slip phenomenon is described from a macroscopic perspective. When flow averaged over the microscale is considered, the resultant slip length is known as the effective slip length [3,4].

Studies on interfacial slip abound in the literature; see Lee *et al.* [5] for a recent review. The effective slip length has been shown to be a function of many geometrical as well as hydrodynamic parameters. A classical work is due to Philip [6], who derived analytical solutions, using conformal mapping, for Stokes flows satisfying mixed no-slip and no-shear boundary conditions. From his solutions, one may deduce, among others, the effective slip length for Stokes flow over a surface patterned with a regular array of longitudinal or transverse no-shear stripes. Such striped stick-slip surfaces have been studied extensively as one of the simplest models for a superhydrophobic surface; see, e.g., Refs. [7,8] and the references therein. The existing studies on effective slip length, including Philip's analytical formulas, are for flow in a nonrotating system. When the system becomes noninertial as it rotates, how the effective slip length may change because of the system rotation remains largely unknown to this date.

The increasing popularity of centrifugal microfluidics [9] has prompted researchers to study flow in rotating microchannels in recent years. Wang [10] pioneered a study on Poiseuille and Couette flows under the effect of boundary slip in a rotating channel. Shit *et al.* [11] also considered slip in their study on electro-osmotic flow in a rotating microchannel. In these studies, the authors have assumed that the slip length is a constant, unaffected by the system rotation.

Ng [12] has recently shown that, if the slip arises from a thin near-wall depletion or lubricating layer, the leading-order slip length is indeed unaffected by the system rotation; it is equal to the thickness of the depletion layer multiplied by the viscosity ratio [13]. The slip length at the second order is, however, a complex function of the rotation speed, implying that the slip length may depend not only on the rotation rate but also on the direction of flow relative to the forcing. Regardless of the isotropy of the wall surface, the slip length for the primary flow can differ from that for the secondary flow.

The need for a further understanding about effective slip in a rotating environment has motivated the present study. We aim to investigate in this paper the effective slip in a channel

---

[*] cong@hku.hk

bounded by micropatterned surfaces and the channel may undergo rotation about an axis perpendicular to its own axis. The specific problem is to consider pressure-driven flow in a parallel-plate channel, which rotates at a constant speed about an axis normal to the plates. The two plates are identically micropatterned featuring a regular array of no-shear alternating with no-slip stripes, and the applied pressure gradient can be in a direction parallel or normal to the stripes. Primary (or axial) flow occurs along the direction of the pressure gradient, while secondary (or transverse) flow caused by Coriolis force will happen in a direction perpendicular to the applied pressure gradient. Our objective is to find out how the effects due to wall slip on the primary and secondary flows are possibly affected by the system rotation.

To facilitate analytical analysis, flow of a low Rossby number is assumed so that the nonlinear inertia can be ignored. In the present problem, the flow is under the combined action of pressure gradient, Coriolis force, and viscous force, subject to mixed no-shear and no-slip boundary conditions. Also assuming steady and fully developed flow, the problem is mathematically formulated in terms of the primitive variables, including three velocity components and pressure, as functions of two-dimensional rectangular coordinates. By virtue of periodicity, the solutions are expressible by eigenfunction expansions, where the unknown coefficients can be determined by point matching the mixed no-shear and no-slip conditions on the boundary. Part of our analysis resembles that presented by Ng and Qi [14], who studied electro-osmotic flow in a rotating rectangular microchannel.

We shall look into various limiting cases, so as to reveal how rotation may give rise to maximum possible change to the flow under the effect of slip. Unlike the case of zero rotation, increasing the no-shear fraction of the wall does not necessarily increase the flow rate in a rotating channel. At low rotation, the axial flow maintains the Poiseuille parabolic profile and the no-shear part of the wall serves to reduce wall resistance, and hence increasing the fraction of the no-shear wall will increase the flow rate. At high rotation, the axial flow structure will change to a boundary-layer type: an Ekman layer near the wall and a geostrophic core in the interior [15]. In the absence of a transverse pressure gradient, the primary flow velocity is zero in the geostrophic core, and hence the primary flow solely relies on Ekman pumping at high rotation. An Ekman layer, however, cannot develop near a no-shear wall. Therefore, increasing the no-shear fraction of the wall amounts to reducing the Ekman pumping. This explains why as the no-shear fraction tends to unity, the primary flow rate will drop to zero at any nonzero rotation rate. Owing to the dramatic change in the primary flow structure, the effective slip length for the primary flow may decrease significantly as the rotation rate increases.

II. PROBLEMS AND SOLUTIONS

As shown in Fig. 1, we consider pressure-driven flow through a parallel-plate channel that is rotating about an axis normal to the channel walls, which are each a superhydrophobic surface patterned with no-shear alternating with no-slip stripes. For simplicity of analysis, an in-phase or symmetric alignment of identical patterns on the two walls is considered.

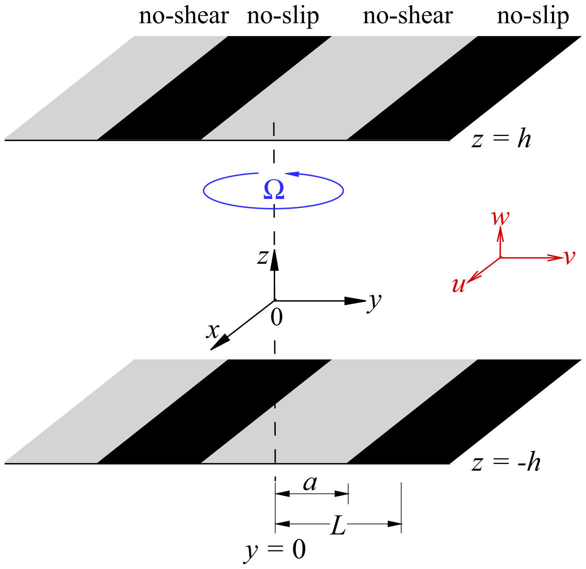

FIG. 1. Definition sketch of the problem: pressure-driven flow through a parallel-plate channel rotating about an axis perpendicular to its walls, which are each patterned with no-shear alternating with no-slip stripes.

The walls are separated by a distance $2h$ apart, and the period of the wall pattern is $2L$, within which $2a$ is the width of a no-shear stripe. Right-handed rectangular coordinates (x,y,z) are defined such that the origin is positioned halfway between the centerlines of two opposite no-shear stripes. While the z axis is perpendicular to the channel walls, the x and y axes are in a direction parallel and normal to the wall stripes, respectively. The system rotates at a constant angular velocity Ω (positive if counterclockwise) about an axis parallel to z. Flow is driven by a pressure gradient that is applied either along the x or the y direction.

On ignoring gravity and inertia (assuming a very small Rossby number), the governing equations for steady pressure-driven flow in the rotating frame is

$$\nabla \cdot \vec{V} = 0, \tag{1}$$

$$2\rho\vec{\Omega} \times \vec{V} = -\nabla p + \mu\nabla^2\vec{V} + \vec{K}. \tag{2}$$

In these equations, $\vec{V} = (u,v,w)$ is the velocity seen in the rotating frame, $\vec{\Omega} = (0,0,\Omega)$, p is the modified pressure, and ρ and μ are the density and dynamic viscosity of the fluid, respectively. The forcing $\vec{K} = (K_x,K_y,0)$ consists of the applied pressure gradients in the x and y directions.

A. Forcing parallel to stripes

Let us first consider flow being driven by a pressure gradient applied purely along the x direction, i.e., parallel to the stripes. Hence, $K_y = 0$. The following normalized variables are introduced:

$$(\hat{x},\hat{y},\hat{z},\hat{a},\hat{h}) = (x,y,z,a,h)/L, \quad (\hat{u},\hat{v},\hat{w}) = (u,v,w)/U,$$
$$\hat{p} = p/(K_x L), \tag{3}$$

where $U \equiv K_x L^2/\mu$ is the velocity scale. For fully developed flow, the flow field is a function of (y,z) only. Hence, in terms of the normalized variables, the governing equations have the following nondimensional component form:

$$-\omega\hat{v} = 1 + \frac{\partial^2\hat{u}}{\partial\hat{y}^2} + \frac{\partial^2\hat{u}}{\partial\hat{z}^2}, \tag{4}$$

$$\omega\hat{u} = -\frac{\partial\hat{p}}{\partial\hat{y}} + \frac{\partial^2\hat{v}}{\partial\hat{y}^2} + \frac{\partial^2\hat{v}}{\partial\hat{z}^2}, \tag{5}$$

$$0 = -\frac{\partial\hat{p}}{\partial\hat{z}} + \frac{\partial^2\hat{w}}{\partial\hat{y}^2} + \frac{\partial^2\hat{w}}{\partial\hat{z}^2}, \tag{6}$$

$$\frac{\partial\hat{v}}{\partial\hat{y}} + \frac{\partial\hat{w}}{\partial\hat{z}} = 0, \tag{7}$$

where

$$\omega = \frac{2\rho\Omega L^2}{\mu} \tag{8}$$

is the rotation parameter. In this problem, primary flow of velocity $u(y,z)$ is driven by the applied pressure gradient in the x direction. Secondary flow of velocity components $v(y,z)$, $w(y,z)$ arises because of the Coriolis acceleration, the terms on the left-hand sides of Eqs. (4) and (5). The flow is to satisfy mixed no-shear and no-slip boundary conditions on the walls:

$$\left.\begin{array}{ll} \partial\hat{u}/\partial\hat{z} = \partial\hat{v}/\partial\hat{z} = 0 & \text{on } 0 \leqslant \hat{y} < \hat{a} \\ \hat{u} = \hat{v} = 0 & \text{on } \hat{a} < \hat{y} \leqslant 1 \end{array}\right\}, \quad \hat{z} = \pm\hat{h}. \tag{9}$$

Assuming impermeable walls, the normal velocity vanishes on the walls

$$\hat{w} = 0 \quad \text{on } \hat{z} = \pm\hat{h}. \tag{10}$$

Let us for simplicity omit the overhead carets from here onward. By virtue of symmetry about the y and z axes and the periodicity, the general solution to the equations above can be written as follows:

$$u(y,z) = b_1\cosh(\phi z)\cos(\phi z) + b_2\sinh(\phi z)\sin(\phi z) + \sum_{n=1}^{\infty} U_n(z)\cos(\alpha_n y), \tag{11}$$

$$v(y,z) = -1/\omega + b_1\sinh(\phi z)\sin(\phi z) - b_2\cosh(\phi z)\cos(\phi z) + \sum_{n=1}^{\infty} V_n(z)\cos(\alpha_n y), \tag{12}$$

$$w(y,z) = \sum_{n=1}^{\infty} W_n(z)\sin(\alpha_n y), \tag{13}$$

$$p(y,z) = \sum_{n=1}^{\infty} P_n(z)\sin(\alpha_n y), \tag{14}$$

where $b_{1,2}$ are undetermined coefficients, $\phi = (\omega/2)^{1/2}$, and $\alpha_n = n\pi$ for $n = 1,2,\cdots$. The physical meaning of the parameter ϕ is noteworthy. From Eq. (8), we can see that it represents a length ratio:

$$\phi = \left(\frac{\omega}{2}\right)^{1/2} = \frac{L}{\delta_E}, \tag{15}$$

where

$$\delta_E = \left(\frac{\mu}{\rho\Omega}\right)^{1/2} \tag{16}$$

is known as the Ekman layer thickness. Hence, ϕ can be interpreted as the inverse Ekman layer thickness normalized by the period of the wall pattern. The effect of the Ekman layer will be discussed later.

Further details of finding the solutions are provided in Appendix A. In particular, the functions $U_n(z)$, $V_n(z)$, and $W_n(z)$ are given in Eqs. (A20)–(A22), and the unknown coefficients, including b_1 and b_2, are determined using the method of point match to satisfy the mixed boundary conditions.

Having solved for $u(y,z)$ and $v(y,z)$, the mean velocities of the primary and secondary flows can be evaluated as follows:

$$\begin{aligned} \bar{u}^{\parallel} &= \frac{1}{h}\int_0^h\int_0^1 u\,dy\,dz \\ &= \frac{1}{2\phi h}[(b_1 + b_2)\cosh(\phi h)\sin(\phi h) \\ &\quad + (b_1 - b_2)\sinh(\phi h)\cos(\phi h)], \end{aligned} \tag{17}$$

$$\begin{aligned} \bar{v}^{\parallel} &= \frac{1}{h}\int_0^h v|_{y=0}\,dz \\ &= -\frac{1}{\omega} + \frac{1}{2\phi h}[(b_1 - b_2)\cosh(\phi h)\sin(\phi h) \\ &\quad - (b_1 + b_2)\sinh(\phi h)\cos(\phi h)], \end{aligned} \tag{18}$$

where we have used an overbar to denote cross-sectional averaging, and the superscript "‖" to denote the forcing being parallel to the stripes.

In terms of the average velocity and velocity gradient over one period of wall pattern, the effective slip lengths for the primary and secondary flows can be found as follows [17]:

$$\eta_x^{\parallel} = -\left.\frac{\langle u\rangle}{\langle\partial u/\partial z\rangle}\right|_{z=h} = -\frac{b_1\cosh(\phi h)\cos(\phi h) + b_2\sinh(\phi h)\sin(\phi h)}{\phi[(b_1 + b_2)\sinh(\phi h)\cos(\phi h) - (b_1 - b_2)\cosh(\phi h)\sin(\phi h)]}, \tag{19}$$

$$\eta_y^{\parallel} = -\left.\frac{\langle v\rangle}{\langle\partial v/\partial z\rangle}\right|_{z=h} = -\frac{-\omega^{-1} + b_1\sinh(\phi h)\sin(\phi h) - b_2\cosh(\phi h)\cos(\phi h)}{\phi[(b_1 - b_2)\sinh(\phi h)\cos(\phi h) + (b_1 + b_2)\cosh(\phi h)\sin(\phi h)]}, \tag{20}$$

where we have used a pair of angle brackets to denote averaging with respect to y only, e.g., $\langle u\rangle \equiv \int_0^1 u\,dy$ and so on.

B. Forcing normal to stripes

Our second problem is to consider flow being driven by a pressure gradient applied purely in the y direction, or

$K_x = 0$. On redefining the velocity scale as $U \equiv K_y L^2/\mu$ and normalizing pressure with respect to $K_y L$, the governing equations in nondimensional form (with the carets omitted) for this problem are

$$-\omega v = \frac{\partial^2 u}{\partial y^2} + \frac{\partial^2 u}{\partial z^2}, \tag{21}$$

$$\omega u = 1 - \frac{\partial p}{\partial y} + \frac{\partial^2 v}{\partial y^2} + \frac{\partial^2 v}{\partial z^2}, \tag{22}$$

$$0 = -\frac{\partial p}{\partial z} + \frac{\partial^2 w}{\partial y^2} + \frac{\partial^2 w}{\partial z^2}, \tag{23}$$

$$\frac{\partial v}{\partial y} + \frac{\partial w}{\partial z} = 0. \tag{24}$$

In this problem, the primary flow is along the y direction (thereby perpendicular to the stripes), while the secondary flow is along the x direction.

Similar to the first problem, the general solution to the present problem is given by

$$u(y,z) = 1/\omega + b_1 \cosh(\phi z)\cos(\phi z) + b_2 \sinh(\phi z)\sin(\phi z) + \sum_{n=1}^{\infty} U_n(z)\cos(\alpha_n y), \tag{25}$$

$$v(y,z) = b_1 \sinh(\phi z)\sin(\phi z) - b_2 \cosh(\phi z)\cos(\phi z) + \sum_{n=1}^{\infty} V_n(z)\cos(\alpha_n y), \tag{26}$$

$$w(y,z) = \sum_{n=1}^{\infty} W_n(z)\sin(\alpha_n y), \tag{27}$$

$$p(y,z) = \sum_{n=1}^{\infty} P_n(z)\sin(\alpha_n y), \tag{28}$$

where $b_{1,2}$ are undetermined coefficients, $\phi = (\omega/2)^{1/2}$, and $\alpha_n = n\pi$ for $n = 1,2,\ldots$. The homogeneous problem being the same, the functions U_n, V_n, and W_n have the same expressions as those given in Eqs. (A20)–(A22). Again, we may use the method of point match to determine the unknown coefficients, as described in Appendix A. Note that the coefficients $b_{1,2}$ here are different in values from their counterparts in the previous problem.

The mean velocities of the primary and secondary flows are given by

$$\begin{aligned}\bar{v}^{\perp} &= \frac{1}{h}\int_0^h v|_{y=0} dz \\ &= \frac{1}{2\phi h}[(b_1 - b_2)\cosh(\phi h)\sin(\phi h) \\ &\quad - (b_1 + b_2)\sinh(\phi h)\cos(\phi h)],\end{aligned} \tag{29}$$

$$\begin{aligned}\bar{u}^{\perp} &= \frac{1}{h}\int_0^h\int_0^1 u dy dz \\ &= \frac{1}{\omega} + \frac{1}{2\phi h}[(b_1 + b_2)\cosh(\phi h)\sin(\phi h) \\ &\quad + (b_1 - b_2)\sinh(\phi h)\cos(\phi h)],\end{aligned} \tag{30}$$

where we have used an overbar to denote cross-sectional averaging, and the superscript "$\perp$" to denote the forcing being normal to the stripes. As will be shown in Sec. III, the primary flow rate is always larger when the forcing is parallel to the stripes than when the forcing is normal to the stripes: $\bar{u}^{\parallel} > \bar{v}^{\perp}$. However, as is mathematically proved in Appendix B, the secondary flow rate is the same irrespective of whether the forcing is parallel or normal to the stripes. We can formally deduce that

$$\bar{u}^{\perp} = -\bar{v}^{\parallel} = \omega\overline{(u^{\parallel} v^{\perp} - u^{\perp} v^{\parallel})}, \tag{31}$$

or the mean secondary flow velocities are equal in magnitude (they are opposite in sign because of the right-hand coordinates). The magnitude of the mean secondary flow velocity is given by the rotation speed multiplied by the difference of the correlation between the primary flow velocities and that between the secondary flow velocities.

Furthermore, the effective slip lengths for the primary and secondary flows can be found as follows:

$$\eta_y^{\perp} = -\left.\frac{\langle v\rangle}{\langle \partial v/\partial z\rangle}\right|_{z=h} = -\frac{b_1 \sinh(\phi h)\sin(\phi h) - b_2 \cosh(\phi h)\cos(\phi h)}{\phi[(b_1 - b_2)\sinh(\phi h)\cos(\phi h) + (b_1 + b_2)\cosh(\phi h)\sin(\phi h)]}, \tag{32}$$

$$\eta_x^{\perp} = -\left.\frac{\langle u\rangle}{\langle \partial u/\partial z\rangle}\right|_{z=h} = -\frac{\omega^{-1} + b_1 \cosh(\phi h)\cos(\phi h) + b_2 \sinh(\phi h)\sin(\phi h)}{\phi[(b_1 + b_2)\sinh(\phi h)\cos(\phi h) - (b_1 - b_2)\cosh(\phi h)\sin(\phi h)]}, \tag{33}$$

where we have used a pair of angle brackets to denote averaging with respect to y only, e.g., $\langle v\rangle \equiv \int_0^1 v dy$ and so on.

C. Limiting cases

1. *Nonrotating channel*

In a nonrotating thick channel, i.e., $\omega = 0$ and $h \gg 1$, the effective slip lengths reduce to those for Stokes flow over a surface with longitudinal and transverse no-shear or no-slip stripes, of which analytical formulas [6] are available as follows:

$$\lim_{\substack{\omega \to 0 \\ h \gg 1}} \eta^{\parallel} = 2 \lim_{\substack{\omega \to 0 \\ h \gg 1}} \eta^{\perp} = \frac{2}{\pi} \ln\left[\sec\left(\frac{\pi a}{2}\right)\right]. \tag{34}$$

In this particular case, the longitudinal slip length is exactly twice the transverse slip length. We shall show that, for $\omega \to 0$

and $h \gg 1$, our numerical results agree with these analytical formulas.

Note that in a nonrotating channel, the effective slip lengths will blow up logarithmically as the no-shear area fraction tends to unity, $a \to 1$. The axial flow rate will accordingly tend to infinity, although in a slow logarithmic fashion, as the walls approach the limit of being fully no-shear. This is expected, since no finite flow is possible without wall resistance balancing the pressure gradient.

2. *Fully no-slip walls*

When the walls are fully no-slip surfaces, $a = 0$, the axial and transverse flow velocities simplify to the following expressions (for applied pressure gradient in the x direction):

$$\lim_{a\to 0} u(z) = \frac{\sinh(\phi h)\sin(\phi h)\cosh(\phi z)\cos(\phi z) - \cosh(\phi h)\cos(\phi h)\sinh(\phi z)\sin(\phi z)}{\omega[\cosh^2(\phi h)\cos^2(\phi h) + \sinh^2(\phi h)\sin^2(\phi h)]}, \tag{35}$$

$$\lim_{a\to 0} v(z) = -\frac{1}{\omega} + \frac{\sinh(\phi h)\sin(\phi h)\sinh(\phi z)\sin(\phi z) + \cosh(\phi h)\cos(\phi h)\cosh(\phi z)\cos(\phi z)}{\omega[\cosh^2(\phi h)\cos^2(\phi h) + \sinh^2(\phi h)\sin^2(\phi h)]}, \tag{36}$$

which accord with the classical solution obtained by Vidyanidhu and Nigam [16].

In the absence of rotation, $\omega \to 0$, the expressions above will further reduce to $u(z) = (h^2 - z^2)/2$ and $v(z) = 0$, the well-known solution for Poiseuille flow between two nonrotating no-slip parallel plates.

On the other extreme, at a very high rotation speed such that the Ekman layer thickness is much thinner than the channel height, or $\phi h \gg 1$, a boundary-layer flow structure will take shape. Viscous effect, and hence velocity shear, is confined to a near-wall boundary layer, known as the Ekman layer, while flow in the interior is essentially nonviscous, known as the geostrophic core. One can easily deduce the following axial and transverse velocities for the Ekman layer near the upper wall ($z = h$):

$$\lim_{\substack{a\to 0\\ \phi h \gg 1}} u(z) = \omega^{-1} e^{-\phi(h-z)} \sin[\phi(h-z)], \tag{37}$$

$$\lim_{\substack{a\to 0\\ \phi h \gg 1}} v(z) = \omega^{-1}\{e^{-\phi(h-z)} \cos[\phi(h-z)] - 1\}. \tag{38}$$

Outside the Ekman layer is the geostrophic core, where the axial velocity is zero, $u = 0$, and the transverse velocity is a nonzero constant, $v = -\omega^{-1}$, a mere balance between Coriolis force and pressure gradient. See Figs. 4(b), 4(c) or 5(b), 5(c) for typical axial and transverse velocity profiles produced by Eqs. (37) and (38). From these equations, one can estimate that the axial velocity should attain its maximum at $\phi(h - z) = \pi/4$, while the transverse velocity will reach its peak magnitude at $\phi(h - z) = 5\pi/4$. The axial velocity also has an overshoot with the maximum negative velocity at $\phi(h - z) = 3\pi/4$.

3. *Fully no-shear walls*

It is easy to show that, for $\omega \neq 0$, the coefficients b_1, b_2 are both zero when the walls are fully no-shear surfaces, $a \to 1$. Consequently, in order to satisfy zero velocity gradients everywhere on the walls, the primary and secondary flow fields (for applied pressure gradient in the x direction) will greatly reduce to

$$\lim_{\substack{a\to 1\\ \omega \neq 0}} u(z) = 0, \tag{39}$$

$$\lim_{\substack{a\to 1\\ \omega \neq 0}} v(z) = -\omega^{-1}. \tag{40}$$

In the presence of rotation, the axial flow will vanish while the transverse flow will maintain a finite uniform velocity under the no-shear boundary condition. This is in sharp contrast to the case of zero rotation. As discussed above, when $\omega = 0$, the axial velocity will not be finite when the boundaries are completely no-shear. These qualitatively different limiting flow fields as $a \to 1$, depending on whether $\omega \neq 0$ or $\omega = 0$, will be further examined below.

III. RESULTS AND DISCUSSION

We first look into how the no-shear area fraction of the wall, a, may affect the cross-sectional mean velocities in the presence of rotation. It is well known that increasing the no-shear fraction, which amounts to increasing the effective slip length of the wall, will always increase the rate of flow in a nonrotating channel. This is not necessarily true in a rotating channel. Typical results are shown in Fig. 2, which reveals trends similar to those previously reported by Wang [10]. While the primary flow velocity decreases monotonically as the rotation rate increases, the secondary flow velocity is a nonmonotonic function of the rotation speed.

The primary flow velocity tends to decrease very sharply as ω increases. It appears from Fig. 2 that a larger no-shear fraction may result in a larger primary flow rate at low rotation, while the effect is opposite, i.e., a smaller primary flow rate, at high rotation, as has been remarked before by Wang [10]. This effect of a on the primary flow rate, however, needs to be examined in greater detail. We shall further discuss this point below.

The secondary flow exhibits a different trend. The secondary flow velocity is exactly zero at $\omega = 0$, and will diminish according to ω^{-1} at large ω. Therefore, there is an intermediate rotation speed ($\omega \approx 2$–10 for $a = 0.9$–0) at which the secondary flow velocity is maximum in magnitude.

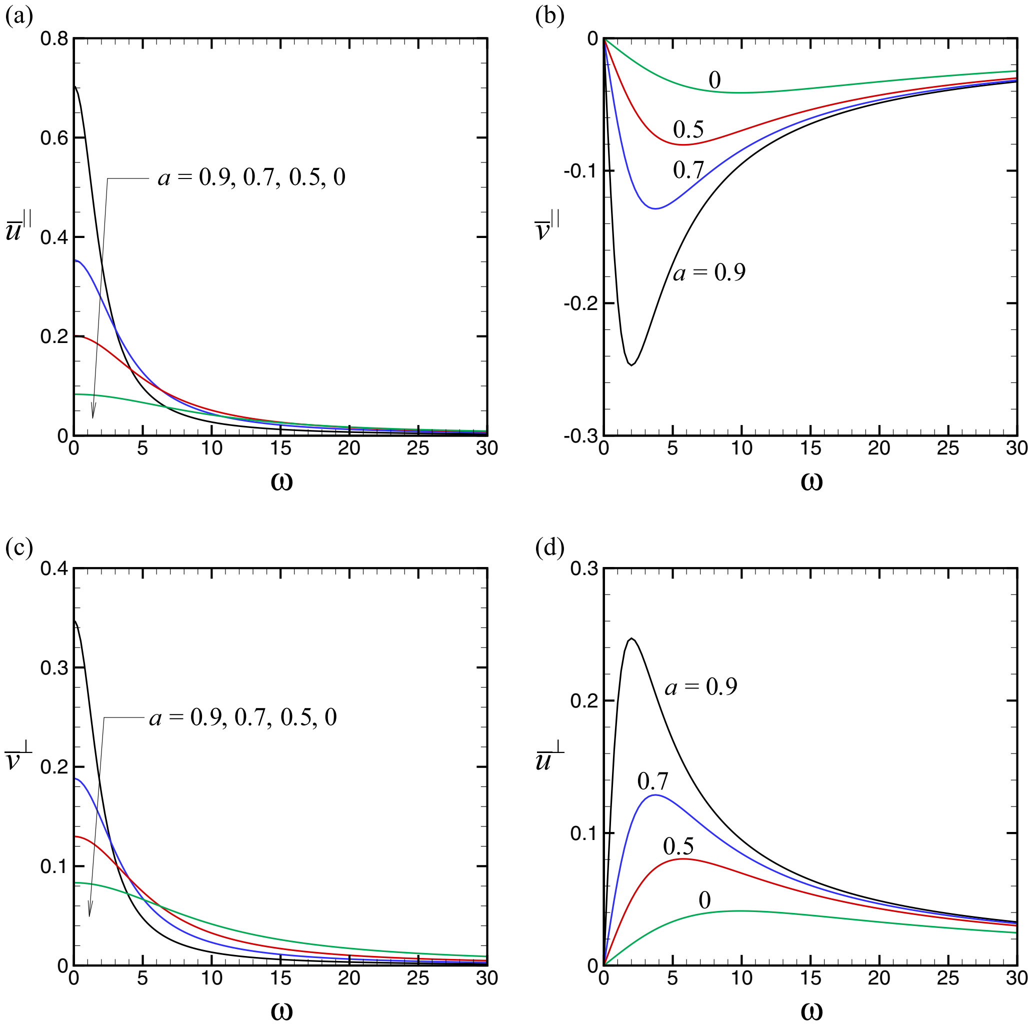

FIG. 2. Cross-sectional mean velocities of primary ($\bar{u}^{\parallel}$ and $\bar{v}^{\perp}$) and secondary ($\bar{v}^{\parallel}$ and $\bar{u}^{\perp}$) flows as functions of the rotation speed ω, for $a = 0,0.5,0.7,0.9$, and $h = 0.5$. The pressure gradient is applied parallel to the stripes in (a), (b), and normal to the stripes in (c), (d).

For either primary or secondary flow, the enhancing effect of the no-shear fraction is most pronounced in a range of the rotation speed where the flow rate is close to the maximum. The no-shear fraction will lose its effect at large ω, suggesting that the mean flow is increasingly insensitive to the boundary condition as the rotation rate increases.

The numerical results shown in Fig. 2 also confirm our earlier remarks. First, the mean primary flow velocity is larger when the forcing is parallel to the stripes than when the forcing is normal to the stripes, or $\bar{u}^{\parallel} > \bar{v}^{\perp}$ for $1 > a > 0$. This outcome is expected as it is consistent with the well-known fact that resistance to flow is smaller in the former than in the latter. Second, the mean secondary flow velocities for the two cases are equal in magnitude and opposite in sign: $\bar{v}^{\parallel} = -\bar{u}^{\perp}$, in spite of the different orientations of the wall pattern in the two cases. This confirms Eq. (31) that we have formally deduced in Appendix B.

It is of particular interest to find out how the flow will depend on the rotation rate as the no-shear fraction approaches the limit of unity. We show in Fig. 3 the cross-sectional mean velocities of the primary and secondary flow as functions of $0 \leqslant a \leqslant 1$ for $\omega \geqslant 0$, where $h = 0.5$. The figure confirms the singular nature of the limiting flow field that we have discussed above. The primary flow velocity will tend to infinity, although in a slow logarithmic manner, as $a \to 1$ when $\omega = 0$. In sharp contrast, the primary flow velocity will drop to zero as $a \to 1$ when $\omega \neq 0$, which accords with Eq. (39). Such dropping off to zero can be very abrupt for small but nonzero ω. For example, in the case of $\omega = 1$, the primary flow velocity keeps increasing with a toward 1 and then drops precipitately to 0 as a gets very close to 1. On the other hand, the secondary flow is identically zero at $\omega = 0$, but since its mean velocity magnitude is given by ω^{-1} at $a = 1$ when $\omega \neq 0$, as in Eq. (40), there can be a sharp increase in the secondary flow rate when ω slightly deviates from 0 and a is close to 1. In other words, in a channel bounded by nearly perfectly slipping walls (say, $a = 0.99$), there will be, respectively, a large decrease or increase in the primary or secondary flow velocities on the inception of rotation, say as the rotation rate ω slightly changes from 0 to 1.

Figure 3 also reveals that, for any $\omega \neq 0$, the mean primary flow velocity is in fact not a monotonic function of a. There always exists an optimum value of a at which the primary flow velocity is maximum. This arises from the fact that the no-shear fraction of the wall has two opposite effects on the

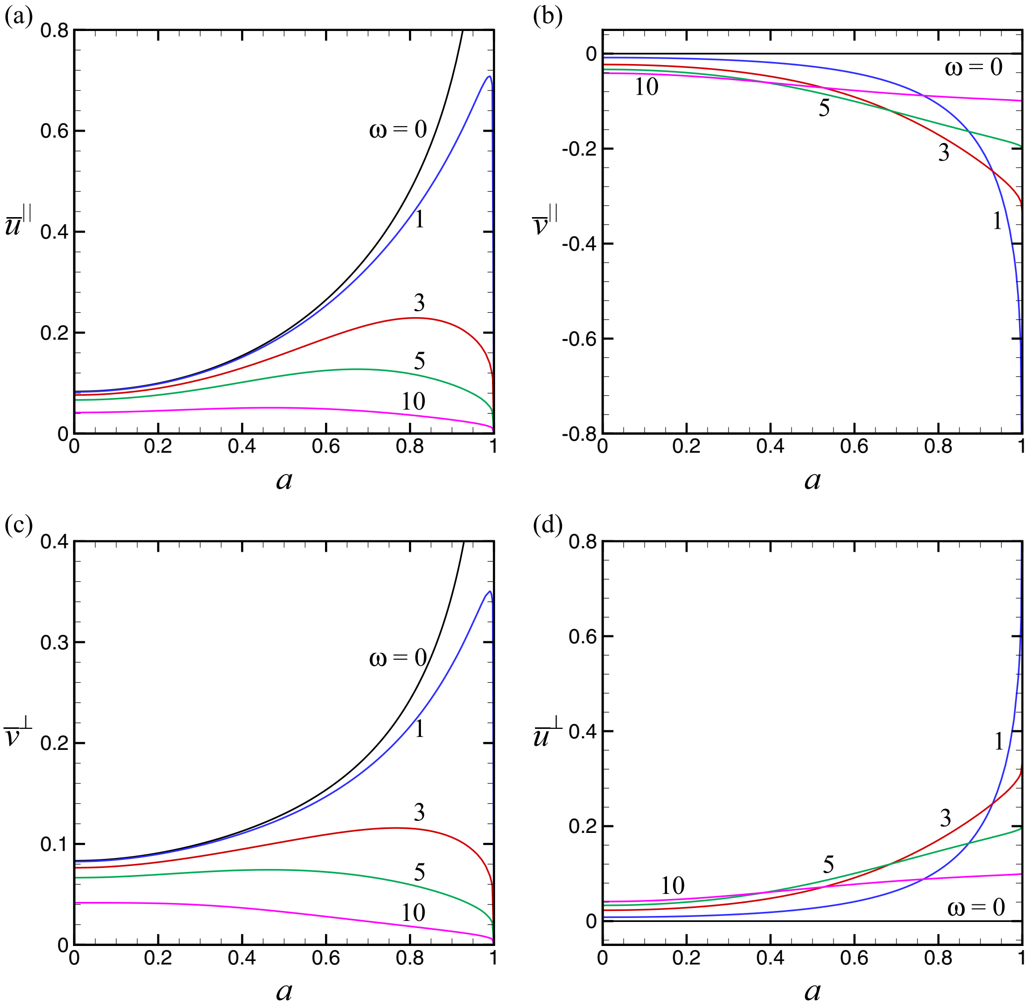

FIG. 3. Cross-sectional mean velocities of primary ($\bar{u}^{\parallel}$ and $\bar{v}^{\perp}$) and secondary ($\bar{v}^{\parallel}$ and $\bar{u}^{\perp}$) flows as functions of the no-shear area fraction a, for $\omega = 0,1,3,5,10$, and $h = 0.5$. The pressure gradient is applied parallel to the stripes in (a), (b), and normal to the stripes in (c), (d).

mean flow. On the one hand, increasing the no-shear fraction may reduce the wall resistance, thereby enhancing the flow rate. This effect is dominant at low rotation. On the other hand, since a no-shear boundary cannot develop an Ekman layer, increasing the no-shear fraction will diminish the Ekman pumping, leading to a smaller primary flow rate. This effect is more influential at higher rotation. As a result, the no-shear fraction can have an enhancing effect on the primary flow only when both a and ω are relatively small. When a and ω are both sufficiently large, the no-shear boundary can only have a negative effect on the primary flow rate.

To further illustrate this point, we show in Fig. 4 some isometric views of the axial and transverse flow fields for $a = 0,0.5,0.9$, $\omega = 0,10$, and $h = 5$, where the forcing is parallel to the stripes. In the absence of rotation ($\omega = 0$), there is no secondary flow, and the axial flow is directly forced by the applied pressure gradient, where the maximum velocity is always at the center of the cross section. The boundary slip is simply to reduce the drag on the flow, and hence to increase the velocity across the entire flow section. In the presence of rotation, the axial flow $u^{\parallel}$ is no longer directly forced by the applied pressure gradient. Instead, it is driven by pumping in the Ekman layer. In the rotating cases shown in Fig. 4, the Ekman layer is much thinner than the channel height as $\phi h = (\omega/2)^{1/2} h = 11.2$. Hence, a very clear Ekman layer structure is visible in Fig. 4(b), where $a = 0$. The axial velocity in the Ekman layer, given in Eq. (37), attains the maximum at a distance of $\pi/(4\phi) = 0.35$ from the wall. In the interior, the geostrophic flow is essentially zero, because of the absence of a transverse pressure gradient. Under rotation, the axial flow counts on the wall shear in developing an Ekman layer, where vorticity is produced from the wall, and diffused by viscosity across the layer. Without wall shear, an Ekman layer cannot develop. Over the part of the wall where the flow is in perfect slip, there is no mechanism to produce vorticity from the wall. When a is so small that the drag reduction effect remains dominant, increasing a may increase on average the flow near the wall; see Fig. 4(e). At the same time, increasing a amounts to decreasing the area of the wall near which an Ekman layer may develop. Therefore, when a becomes large, say $a > 0.5$, the Ekman pumping can be much weakened; see Fig. 4(h). For $\omega = 10$, the transverse velocity profiles $v^{\parallel}(y,z)$ are shown in Figs. 4(c), 4(f), 4(i). Again, the classical Ekman layer structure is visible in Fig. 4(c). The transverse flow is essentially driven by the axial pressure gradient. In the geostrophic interior, the limit of $v^{\parallel} = -\omega^{-1} = -0.1$ is clearly seen in all the profiles.

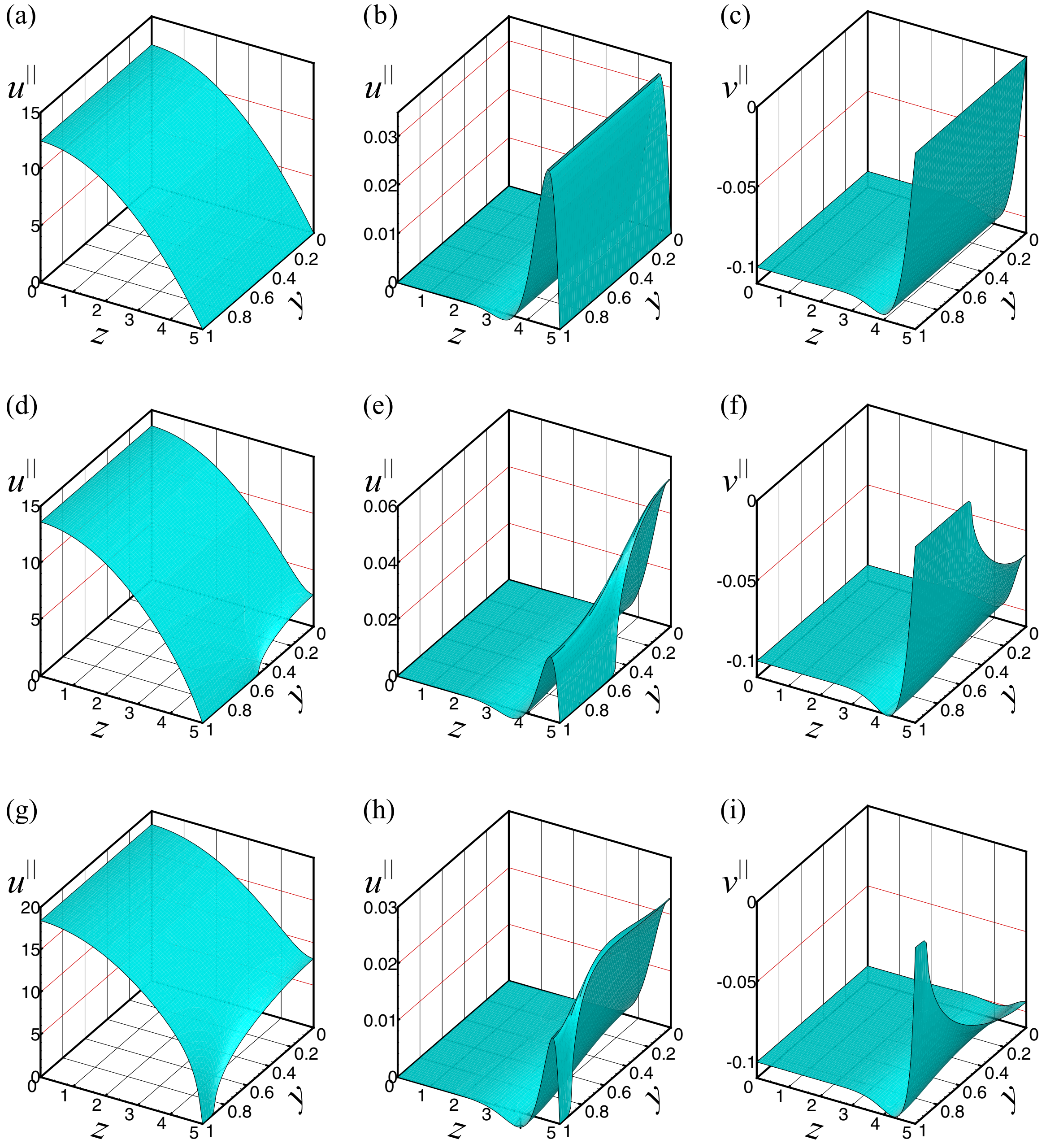

FIG. 4. For forcing parallel to the stripes and $h = 5$: axial velocity profiles $u^{\parallel}(y,z)$ for $\omega = 0$ (nonrotating) in (a) $a = 0$, (d) $a = 0.5$, (g) $a = 0.9$; axial flow velocity profiles $u^{\parallel}(y,z)$ for $\omega = 10$ (rotating) in (b) $a = 0$, (e) $a = 0.5$, (h) $a = 0.9$; transverse flow velocity profiles $v^{\parallel}(y,z)$ for $\omega = 10$ (rotating) in (c) $a = 0$, (f) $a = 0.5$, (i) $a = 0.9$. Note that the wall at $z = 5$ is no-shear in $0 \leqslant y < a$ and no-slip in $a < y \leqslant 1$.

Near the wall, the transverse flow has a sharp velocity gradient, which is followed by a small overshoot before approaching the geostrophic limit. Increasing the no-shear fraction (or reducing the wall resistance) will always enhance transverse flow in the near-wall region, but has no effect on flow in the interior. We may therefore infer from these profiles that, at sufficiently large rotation, the effect of boundary slip is limited to flow in the near-wall region only. This is fundamentally different from the case of nonrotating flow, where the boundary slip may affect the entire flow.

We show in Fig. 5 the transversely averaged (i.e., averaged with respect to y only) velocity profiles $\langle u\rangle^{\parallel}(z)$ and $\langle v\rangle^{\parallel}(z)$, corresponding to the cases shown in Fig. 4. These velocity profiles help us visualize how rotation can fundamentally change the flow structure. In the case of zero rotation ($\omega = 0$), the entire velocity profile is affected by the wall slip. Nevertheless, for any wall slip, the velocity profile keeps the basic parabolic form of Poiseuille flow; see Fig. 5(a). In this case, while the slip velocity increases monotonically with a, the near-wall velocity gradient is not affected by a. It is the ratio of the averaged slip velocity to the averaged velocity gradient at the wall that defines the macroscopic quantity known as effective slip length. Hence, without rotation, the effective slip length can have a relatively simple relationship with the no-shear fraction of the wall: it increases monotonically with a. For flow in a very thick channel or semi-infinite domain, the

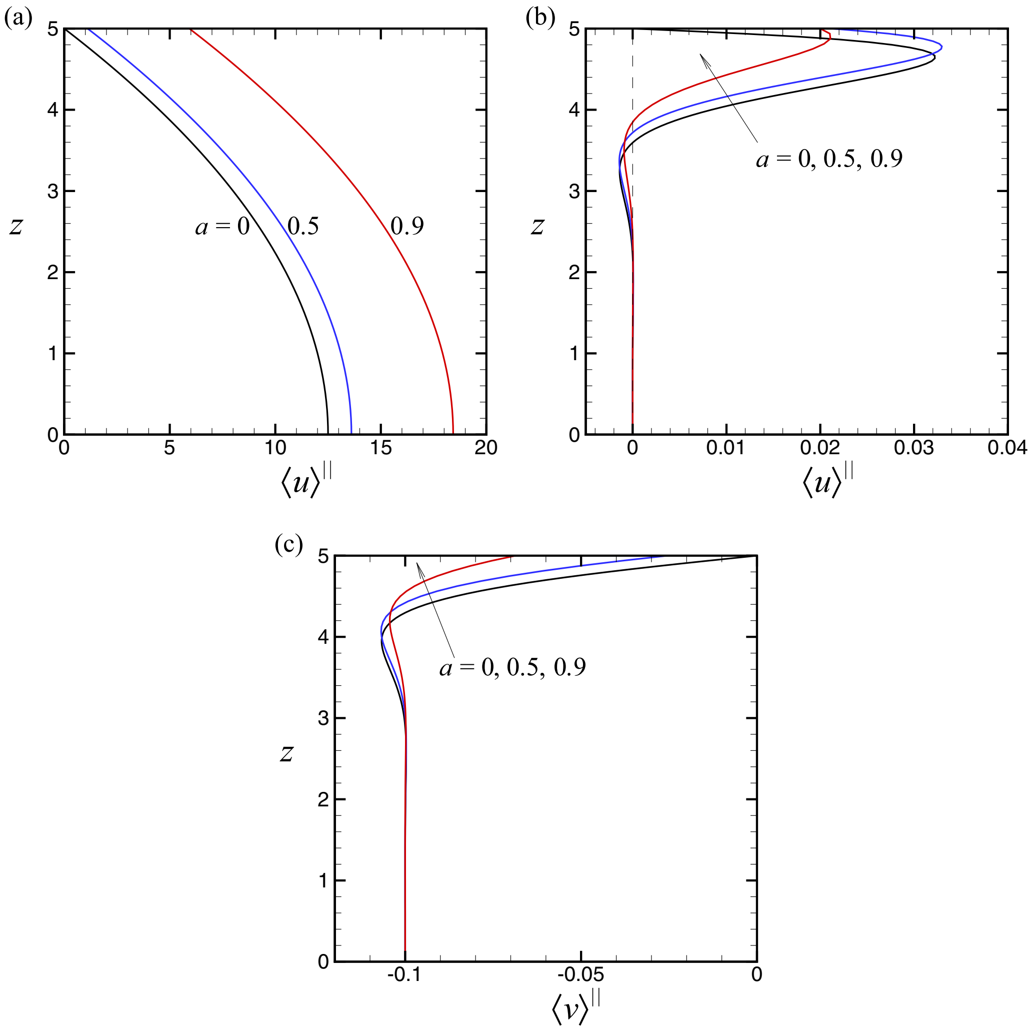

FIG. 5. For forcing parallel to the stripes and $h = 5$, (a) transversely averaged axial velocity profiles $\langle u\rangle^{\parallel}(z)$ for $\omega = 0$ (nonrotating); (b) ditto but for $\omega = 10$ (rotating); (c) transversely averaged transverse velocity profiles $\langle v\rangle^{\parallel}(z)$ for $\omega = 10$ (rotating).

averaged velocity gradient at the wall is also the asymptotic velocity gradient at a sufficiently far distance away from the patterned wall. A far-field velocity gradient amounts to a boundary shear. The effective slip length for nonrotating flow over a patterned surface is therefore the same whether the flow is driven by a pressure gradient (Poiseuille flow) or boundary shear (Couette flow).

In the case of nonzero rotation, not only is the basic flow structure different from that in the case of zero rotation, but also the velocity slip and velocity gradient at the wall can both change with the no-shear fraction. As has been explained above, the axial flow is essentially driven by Ekman pumping, which vanishes when the walls are perfectly slipping $a = 1$. Figure 5(b) clearly shows that flow in the Ekman layer for $a = 0.9$ is weaker than that for $a = 0.5$ or even than that for $a = 0$. The wall slip can have a positive effect on flow in the Ekman layer only when the no-shear fraction is not too large. Furthermore, the nonmonotonic velocity profile in the Ekman layer causes the velocity gradient to change rapidly in this layer. The velocity gradient can change in sign at a short distance from the wall. The so-called far-field velocity gradient is therefore not meaningful in the presence of an Ekman layer. The effective slip length for rotating flow over a patterned surface will depend strongly on the Ekman layer structure developed on the surface, which can be different depending on the forcing type and other conditions. It is possible that Poiseuille flow and Couette flow may produce different values of effective slip length for flow over the same patterned surface in a rotating channel.

Figure 5(c) displays, once again, how the transverse flow in the Ekman layer may change as the no-shear fraction increases. As a increases, the wall slip velocity increases but the near-wall velocity gradient decreases, thereby an increased effective slip length. As has been explained above, the transverse flow will tend to a uniform profile as the no-shear fraction approaches unity. In this limit, the effective slip length for the transverse flow is in theory infinite.

From Figs. 4 and 5, we may infer that, in a rotating channel, the no-shear part of the wall is to affect the primary and secondary flows only in the Ekman layer, but not in the geostrophic core, and the effect can be positive or negative. This is in sharp contrast to the case of a nonrotating flow,

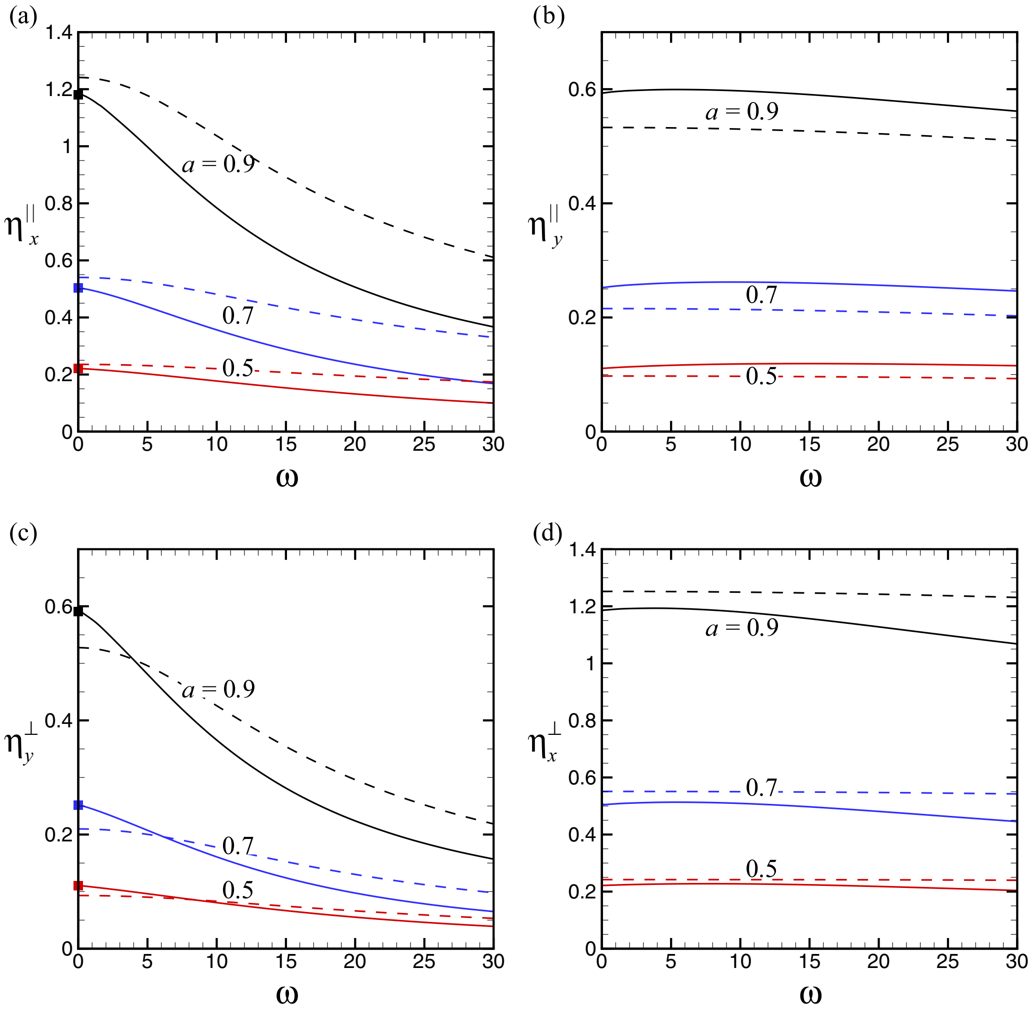

FIG. 6. Effective slip lengths for primary ($\eta_x^{\parallel}$ and $\eta_y^{\perp}$) and secondary ($\eta_y^{\parallel}$ and $\eta_x^{\perp}$) flows as functions of the rotation speed ω, for $a = 0.5, 0.7, 0.9$, and $h = 5$ (solid lines), $h = 0.5$ (dashed lines). The pressure gradient is applied parallel to the stripes in (a), (b), and normal to the stripes in (c), (d). The squares in (a), (c) are from Eq. (34).

where a no-shear wall can have effect across the entire flow, and the effect is always positive.

Let us now look into various effects on the effective slip lengths, which are evaluated using Eqs. (19), (20), (32), and (33). Figure 6 shows the effective slip lengths for the primary and secondary flows as functions of the rotation speed $\omega \geqslant 0$. It is important to note that, in a rotating channel, the effective slip length for flow in different directions will be affected differently by the rotation. The effective slip length for primary flow, whether the forcing is parallel or normal to the stripes, is found to be a strong function of rotation: $\eta_x^{\parallel}$ or $\eta_y^{\perp}$ may decrease appreciably as ω increases. Such decrease of the effective slip length is more pronounced for larger a and/or larger h. The effective slip length for secondary flow also varies with the rotation rate, but in a much milder manner. At $\omega = 30$ and $a = 0.9, h = 5$, $\eta_x^{\parallel}$ decreases by nearly 70%, while $\eta_y^{\parallel}$ decreases only by some 5%, when compared with those at $\omega = 0$. One can ascribe this appreciable change in $\eta_x^{\parallel}$ to the fundamental change in the primary flow structure (from Poiseuille flow to Ekman layer plus geostrophic interior) as ω varies from 0 to 30, as has been discussed above. The secondary flow keeps the basic Ekman layer structure as the rotation speed varies. Therefore, the effective slip length for secondary flow is much less sensitive to the rotation speed. At sufficiently large ω, the slip length for secondary flow can be larger than that for primary flow when the forcing is parallel to the stripes. In Figs. 6(a) and 6(c), we show by the square symbols the values computed by the analytical formulas due to Philip [6], as given in Eq. (34), for $\omega = 0$ and $h \gg 1$. Our results, which are for $h = 5$, are found to be in good agreement with those by the analytical formulas. According to these formulas, the effective slip length for flow over longitudinal stripes is exactly twice that for flow over transverse stripes. Our results reveal that this factor of 2 holds only for the axial flow when the rotation is zero ($\omega = 0$). When $\omega \neq 0$, the ratio of slip lengths, $\eta_x^{\parallel}/\eta_y^{\perp}$ for primary flows or $\eta_x^{\perp}/\eta_y^{\parallel}$ for secondary flows, is in general different from, but close to, the factor of 2.

By relating the mean flow to the slip length, shown in Figs. 2 and 6, respectively, we may further remark that in a rotating environment the slip length does not necessarily have a direct bearing on the flow rate. For example, the secondary flow rate

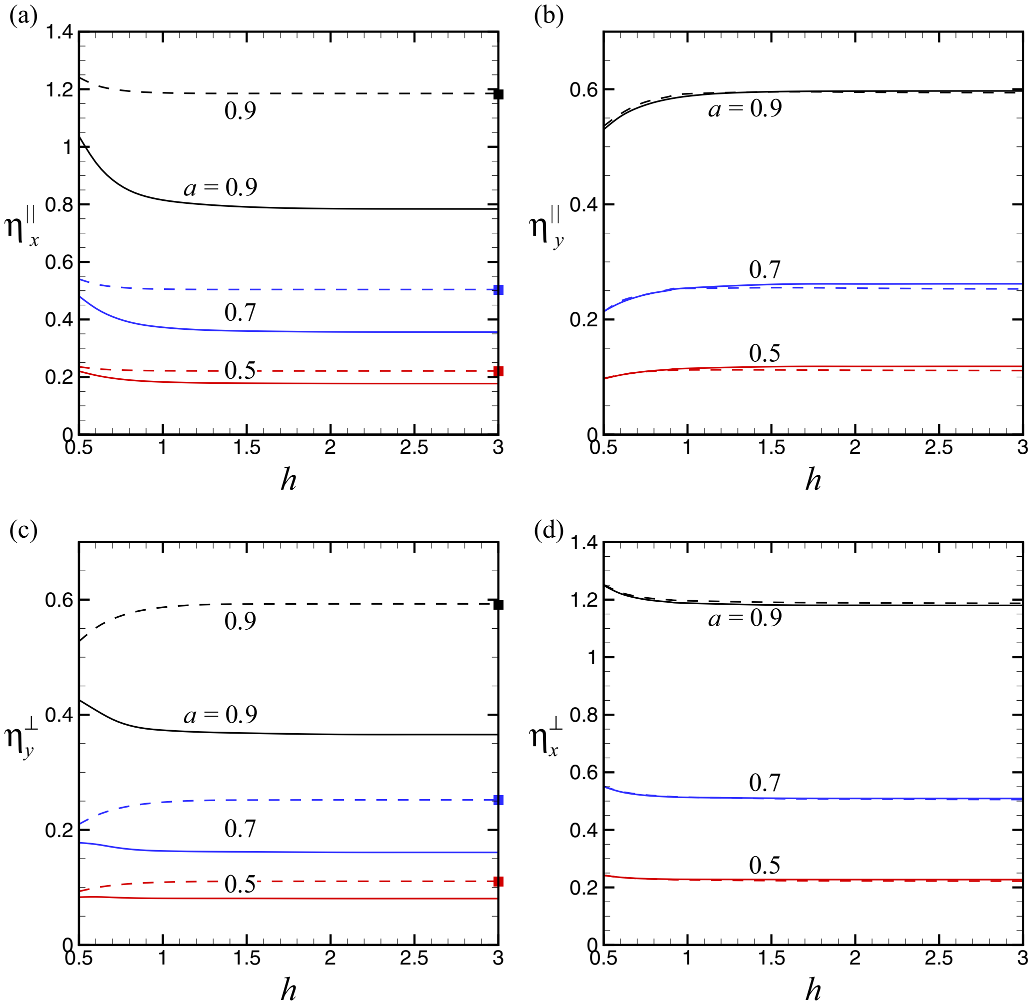

FIG. 7. Effective slip lengths for primary ($\eta_x^{\parallel}$ and $\eta_y^{\perp}$) and secondary ($\eta_y^{\parallel}$ and $\eta_x^{\perp}$) flows as functions of the channel height h, for $a = 0.5, 0.7, 0.9$, and $\omega = 10$ (solid lines), $\omega = 0$ (dashed lines). The pressure gradient is applied parallel to the stripes in (a), (b), and normal to the stripes in (c), (d). The squares in (a), (c) are from Eq. (34).

is the same when the forcing is applied parallel or normal to the stripes ($|\bar{v}^{\parallel}| = |\bar{u}^{\perp}|$), but the corresponding effective slip lengths are not the same ($\eta_y^{\parallel} \neq \eta_x^{\perp}$). This is a consequence of the interaction between the primary and secondary flows; flow in one direction is affected not only by slip in that direction, but also by slip in the orthogonal direction.

We finally show in Fig. 7 the effective slip lengths as functions of the channel height h. Regardless of the channel rotation, the effective slip lengths become insensitive to the channel height for sufficiently large h, say when $h > 2$. From Figs. 7(a) and 7(c), we see that increasing the channel height is always to decrease the slip length for the primary flow in a rotating channel, irrespective of the forcing direction. This is different from the case of a nonrotating channel, for which the longitudinal slip length may decrease, while the transverse slip length may increase, as the channel height increases. The dependence of the slip length for secondary flow on the channel height is not appreciably affected by the rotation. Again, we show in Figs. 7(a) and 7(c) by the square symbols the analytical values using Eq. (34), for $\omega = 0$ and $h \gg 1$. Our numerical results, which are for a finite channel height $h = 3$, are found to be already in close agreement with the analytical values valid for large h. This suggests that a channel bounded by plane stick-slip walls, a height of $h > 2$ can be considered thick enough for the channel wall confinement to become negligible.

IV. CONCLUDING REMARKS

We have developed semianalytical models, based on the methods of eigenfunction expansion and point match, to describe low-Reynolds-number flow through a parallel-plate channel rotating about an axis perpendicular to its walls, which are patterned with a periodic array of no-shear alternating with no-slip stripes. The flow is driven by a pressure gradient that is parallel or normal to the stripes. The present problem is controlled by three parameters: the rotation speed, the no-shear area fraction of the wall, and the channel height. Some key findings are summarized as follows. First, the rotation is always to decrease the primary flow rate, while there exists an optimum rotation rate at which the secondary flow rate is maximum. At high rotation, the secondary flow rate is scaled by the inverse of the rotation speed. Second, at the limit of the walls being perfectly slipping, the flow fields will have dramatically different structures, depending on whether the rotation is zero or not. Without rotation, the primary flow is infinitely large, and the secondary flow is zero. With rotation, the primary flow velocity is zero, while the secondary flow velocity is equal in magnitude to the inverse of the rotation speed. Therefore, when the no-shear area fraction of the wall is close to unity, there can be an abrupt change in the primary and secondary flow rates when the rotation speed slightly varies from zero to a small value. Third, for any nonzero rotation rate, there exists an optimum no-shear fraction at which the primary flow rate is maximum. Increasing the no-shear wall area fraction will have two contrasting effects on the primary flow rate: to reduce the wall resistance, and to weaken the Ekman pumping, which are dominant when the rotation rate is low and high, respectively. We have also mathematically shown that the secondary flow rate is the same regardless of whether the pressure gradient is applied parallel or normal to the stripes. Fourth, the effective slip lengths for flow in different directions are affected in different manners by the rotation. The effective slip length for primary flow will decrease significantly as the rotation rate increases, but that for secondary flow changes only modestly as the rotation rate varies. One is cautioned that in a rotating environment the slip length is no longer simply related to the flow rate; an increased slip length in one direction does not necessarily lead to an increased flow rate in that direction. In summary, the effective slip arising from flow over a composite surface in a rotating environment can be very different from its zero-rotation counterpart. System rotation will modify the role played by a no-shear boundary in controlling the flow. An important finding of this study is that, in the presence of system rotation, the boundary slip can have effect on flow in the near-wall Ekman layer only, but not on flow in the core region.

ACKNOWLEDGMENTS

Comments by the reviewer are gratefully acknowledged. Financial support was given by the Research Grants Council of the Hong Kong Special Administrative Region, China, through General Research Fund Project No. 17206615.

APPENDIX A

On substituting Eqs. (11)–(14) for the velocities and pressure into Eqs. (4)–(7), we get after some algebra

$$U_n^{(6)} - 3\alpha_n^2 U_n^{(4)} + \left(3\alpha_n^4 + \omega^2\right)U_n'' - \alpha_n^6 U_n = 0, \tag{A1}$$

$$V_n = \omega^{-1}\left(-U_n'' + \alpha_n^2 U_n\right), \tag{A2}$$

$$W_n = \alpha_n^{-3}\left(\omega U_n' + 2\alpha_n^2 V_n' - V_n'''\right), \tag{A3}$$

$$P_n = \alpha_n^{-1}\left(V_n'' - \alpha_n^2 V_n - \omega U_n\right). \tag{A4}$$

As in Ng and Qi [14], on letting $U_n = \exp(\lambda z)$, we obtain from Eq. (A1) the following characteristic equation

$$\lambda^6 - 3\alpha_n^2\lambda^4 + \left(3\alpha_n^4 + \omega^2\right)\lambda^2 - \alpha_n^6 = 0. \tag{A5}$$

The six roots of this equation are

$$\lambda = \pm\lambda_n, \quad \lambda = \pm\sigma_n \pm \mathrm{i}\xi_n, \tag{A6}$$

where $\mathrm{i} = \sqrt{-1}$ is the complex unit,

$$\lambda_n = \left[\alpha_n^2 + S_n + T_n\right]^{1/2}, \tag{A7}$$

and

$$\sigma_n = \left[\frac{1}{2}\left(f_n + \sqrt{f_n^2 + g_n^2}\right)\right]^2, \quad \xi_n = \frac{g_n}{2\sigma_n}, \tag{A8}$$

in which

$$f_n = \alpha_n^2 - \frac{1}{2}(S_n + T_n), \quad g_n = \frac{\sqrt{3}}{2}(S_n - T_n), \tag{A9}$$

$$S_n = \left[-\frac{\omega^2\alpha_n^2}{2} + \sqrt{\left(\frac{\omega^2}{3}\right)^3 + \left(\frac{\omega^2\alpha_n^2}{2}\right)^2}\,\right]^{1/3}, \tag{A10}$$

$$T_n = -\left[\frac{\omega^2\alpha_n^2}{2} + \sqrt{\left(\frac{\omega^2}{3}\right)^3 + \left(\frac{\omega^2\alpha_n^2}{2}\right)^2}\,\right]^{1/3}. \tag{A11}$$

Note that $\alpha_n^2 + S_n + T_n$ is always positive, and therefore λ_n is always a real quantity.

By symmetry about $z = 0$, U_n is an even function of z, and hence, we may write

$$\begin{aligned} U_n = {} & C_{1n}\frac{\cosh(\lambda_n z)}{\cosh(\lambda_n h)} + C_{2n}\frac{\cosh(\sigma_n z)}{\cosh(\sigma_n h)}\cos(\xi_n z) \\ & + C_{3n}\frac{\sinh(\sigma_n z)}{\sinh(\sigma_n h)}\sin(\xi_n z), \end{aligned} \tag{A12}$$

where $C_{1n,2n,3n}$ are undetermined coefficients. From Eqs. (A2) and (A3), we further get

$$\begin{aligned} V_n = {} & C_{1n}A_{1n}\frac{\cosh(\lambda_n z)}{\cosh(\lambda_n h)} \\ & + C_{2n}\left[A_{2n}\frac{\cosh(\sigma_n z)}{\cosh(\sigma_n h)}\cos(\xi_n z) + A_{3n}\frac{\sinh(\sigma_n z)}{\cosh(\sigma_n h)}\sin(\xi_n z)\right] \\ & + C_{3n}\left[A_{2n}\frac{\sinh(\sigma_n z)}{\sinh(\sigma_n h)}\sin(\xi_n z) - A_{3n}\frac{\cosh(\sigma_n z)}{\sinh(\sigma_n h)}\cos(\xi_n z)\right], \end{aligned} \tag{A13}$$

$$\begin{aligned} W_n = {} & C_{1n}B_{1n}\frac{\sinh(\lambda_n z)}{\cosh(\lambda_n h)} \\ & + C_{2n}\left[B_{2n}\frac{\sinh(\sigma_n z)}{\cosh(\sigma_n h)}\cos(\xi_n z) + B_{3n}\frac{\cosh(\sigma_n z)}{\cosh(\sigma_n h)}\sin(\xi_n z)\right] \\ & + C_{3n}\left[B_{2n}\frac{\cosh(\sigma_n z)}{\sinh(\sigma_n h)}\sin(\xi_n z) - B_{3n}\frac{\sinh(\sigma_n z)}{\sinh(\sigma_n h)}\cos(\xi_n z)\right], \end{aligned} \tag{A14}$$

where

$$\begin{aligned} & A_{1n} = \left(\alpha_n^2 - \lambda_n^2\right)/\omega, \quad A_{2n} = \left(\alpha_n^2 - \sigma_n^2 + \xi_n^2\right)/\omega, \\ & A_{3n} = 2\sigma_n\xi_n/\omega, \end{aligned} \tag{A15}$$

$$\begin{aligned} & B_{1n} = \alpha_n A_{1n}/\lambda_n, \quad B_{2n} = \alpha_n(\sigma_n A_{2n} - \xi_n A_{3n})/\left(\sigma_n^2 + \xi_n^2\right), \\ & B_{3n} = \alpha_n(\xi_n A_{2n} + \sigma_n A_{3n})/\left(\sigma_n^2 + \xi_n^2\right). \end{aligned} \tag{A16}$$

Using the no-flux boundary condition as in Eq. (10), we may determine

$$C_{1n} = D_{1n}C_{2n} + D_{2n}C_{3n}, \tag{A17}$$

where

$$D_{1n} = -\frac{B_{2n}\tanh(\sigma_n h)\cos(\xi_n h) + B_{3n}\sin(\xi_n h)}{B_{1n}\tanh(\lambda_n h)}, \tag{A18}$$

$$D_{2n} = -\frac{B_{2n}\coth(\sigma_n h)\sin(\xi_n h) - B_{3n}\cos(\xi_n h)}{B_{1n}\tanh(\lambda_n h)}. \tag{A19}$$

On substituting C_{1n} into Eqs. (A12)–(A14), we finally get the following expressions for the three functions:

$$\begin{aligned} U_n(z) = {} & C_{2n}\left[D_{1n}\frac{\cosh(\lambda_n z)}{\cosh(\lambda_n h)} + \frac{\cosh(\sigma_n z)}{\cosh(\sigma_n h)}\cos(\xi_n z)\right] \\ & + C_{3n}\left[D_{2n}\frac{\cosh(\lambda_n z)}{\cosh(\lambda_n h)} + \frac{\sinh(\sigma_n z)}{\sinh(\sigma_n h)}\sin(\xi_n z)\right], \end{aligned} \tag{A20}$$

$$\begin{aligned} V_n(z) = {} & C_{2n}\left[A_{1n}D_{1n}\frac{\cosh(\lambda_n z)}{\cosh(\lambda_n h)} + A_{2n}\frac{\cosh(\sigma_n z)}{\cosh(\sigma_n h)}\cos(\xi_n z) \right. \\ & \left. + A_{3n}\frac{\sinh(\sigma_n z)}{\cosh(\sigma_n h)}\sin(\xi_n z)\right] \\ & + C_{3n}\left[A_{1n}D_{2n}\frac{\cosh(\lambda_n z)}{\cosh(\lambda_n h)} + A_{2n}\frac{\sinh(\sigma_n z)}{\sinh(\sigma_n h)}\sin(\xi_n z) \right. \\ & \left. - A_{3n}\frac{\cosh(\sigma_n z)}{\sinh(\sigma_n h)}\cos(\xi_n z)\right], \end{aligned} \tag{A21}$$

$$\begin{aligned} W_n(z) = {} & C_{2n}\left[B_{1n}D_{1n}\frac{\sinh(\lambda_n z)}{\cosh(\lambda_n h)} + B_{2n}\frac{\sinh(\sigma_n z)}{\cosh(\sigma_n h)}\cos(\xi_n z) \right. \\ & \left. + B_{3n}\frac{\cosh(\sigma_n z)}{\cosh(\sigma_n h)}\sin(\xi_n z)\right] \\ & + C_{3n}\left[B_{1n}D_{2n}\frac{\sinh(\lambda_n z)}{\cosh(\lambda_n h)} + B_{2n}\frac{\cosh(\sigma_n z)}{\sinh(\sigma_n h)}\sin(\xi_n z) \right. \\ & \left. - B_{3n}\frac{\sinh(\sigma_n z)}{\sinh(\sigma_n h)}\cos(\xi_n z)\right], \end{aligned} \tag{A22}$$

If we truncate the coefficients C_{2n} and C_{3n} each to N terms, our remaining task is to determine the $2(n+1)$ coefficients: $b_{1,2}$, $C_{2(1,\cdots,N)}$ and $C_{3(1,\cdots,N)}$, using the mixed no-shear and no-slip conditions at the wall. In this regard, the method of point match is used. We choose $N+1$ evenly spaced points along $z = h$, $0 \leqslant y \leqslant 1$:

$$y_i = (i-1)/N, \quad i = 1, \ldots, N+1. \tag{A23}$$

The mixed conditions in Eq. (9) are then imposed on these points

$$\left.\begin{array}{ll} \partial u/\partial z = \partial v/\partial z = 0 & \text{at } 0 \leqslant y_i < a \\ u = v = 0 & \text{at } a < y_i \leqslant 1 \end{array}\right\}, \quad z = h, \quad i = 1, \ldots, N+1, \tag{A24}$$

which constitutes a system of $2(N+1)$ linear equations for the $2(N+1)$ unknown coefficients. The system of equations can be solved readily by computer using a standard routine. We have used $N \sim 300$ to achieve sufficient accuracy of the results.

APPENDIX B

For flow driven by a unity pressure gradient in a direction parallel to the stripes, the governing equations are

$$\nabla^2 u^{\parallel} + \omega v^{\parallel} = -1, \tag{B1}$$

$$\nabla^2 v^{\parallel} - \omega u^{\parallel} = \frac{\partial p^{\parallel}}{\partial y}, \tag{B2}$$

$$\nabla^2 w^{\parallel} = \frac{\partial p^{\parallel}}{\partial z}, \tag{B3}$$

$$\frac{\partial v^{\parallel}}{\partial y} + \frac{\partial w^{\parallel}}{\partial z} = 0, \tag{B4}$$

where $\nabla \equiv \partial^2/\partial y^2 + \partial^2/\partial z^2$. In this problem, the primary flow ($u^{\parallel}$) is in the x direction, while the secondary flow ($v^{\parallel}$) is in the y direction.

For flow driven by a unity pressure gradient in a direction normal to the stripes, the governing equations are

$$\nabla^2 u^{\perp} + \omega v^{\perp} = 0, \tag{B5}$$

$$\nabla^2 v^{\perp} - \omega u^{\perp} = \frac{\partial p^{\perp}}{\partial y} - 1, \tag{B6}$$

$$\nabla^2 w^{\perp} = \frac{\partial p^{\perp}}{\partial z}, \tag{B7}$$

$$\frac{\partial v^{\perp}}{\partial y} + \frac{\partial w^{\perp}}{\partial z} = 0. \tag{B8}$$

In this problem, the primary flow ($v^{\perp}$) is in the y direction, while the secondary flow ($u^{\perp}$) is in the x direction.

On multiplying Eq. (B1) by $u^{\perp}$, we can get the following:

$$\begin{aligned} & u^{\perp}\nabla^2 u^{\parallel} + \omega u^{\perp} v^{\parallel} = -u^{\perp} \\ & \quad \Rightarrow \nabla \cdot (u^{\perp}\nabla u^{\parallel} - u^{\parallel}\nabla u^{\perp}) + u^{\parallel}\nabla^2 u^{\perp} + \omega u^{\perp} v^{\parallel} = -u^{\perp} \\ & \quad \Rightarrow \nabla \cdot (u^{\perp}\nabla u^{\parallel} - u^{\parallel}\nabla u^{\perp}) + \omega(u^{\perp}v^{\parallel} - u^{\parallel}v^{\perp}) = -u^{\perp}, \end{aligned} \tag{B9}$$

where Eq. (B5) has been used. When integrated over one periodic unit sectional area, $\mathsf{D} = \{y,z| -1 \leqslant y \leqslant 1, -h \leqslant z \leqslant h\}$, the integral of the divergence term in the equation above will vanish, as shown below. Using the divergence theorem,

$$\begin{aligned} & \iint_{\mathsf{D}} \nabla \cdot (u^{\perp}\nabla u^{\parallel} - u^{\parallel}\nabla u^{\perp}) dA \\ & \quad = \int_{\partial\mathsf{D}} (u^{\perp}\nabla u^{\parallel} - u^{\parallel}\nabla u^{\perp}) \cdot \vec{n} dS, \end{aligned} \tag{B10}$$

where $\vec{n}$ is the unit outward normal vector to the boundary $\partial\mathsf{D}$ of the sectional area D. Along the top and bottom boundaries, $z = \pm h$, where the condition is no-slip or no-shear, $u^{\parallel} = u^{\perp} = 0$ or $\partial u^{\parallel}/\partial z = \partial u^{\perp}\partial z = 0$, and hence the integrand of the line integral is zero. Along the lateral boundaries, $y = \pm 1$, which are lines of symmetry, $\partial u^{\parallel}/\partial y = \partial u^{\perp}\partial y = 0$, and hence the integrand of the line integral is zero as well. Therefore, the integrand of the line integral is zero everywhere on $\partial\mathsf{D}$, which implies that

$$\iint_{\mathsf{D}} \nabla\cdot(u^{\perp}\nabla u^{\parallel} - u^{\parallel}\nabla u^{\perp})\,dA = 0. \tag{B11}$$

It follows that, when averaged over D, Eq. (B9) yields

$$\bar{u}^{\perp} = \omega\overline{(u^{\parallel}v^{\perp} - u^{\perp}v^{\parallel})}, \tag{B12}$$

where the overbar denotes the cross-sectional averaging: $\bar{f} \equiv (4h)^{-1}\int_{-h}^{h}\int_{-1}^{1} f\,dy\,dz$ for any function $f(y,z)$.

Next, on multiplying Eq. (B6) by $v^{\parallel}$, we can get the following:

$$\begin{aligned}
&v^{\parallel}\nabla^2 v^{\perp} - \omega u^{\perp}v^{\parallel} = v^{\parallel}\frac{\partial p^{\perp}}{\partial y} - v^{\parallel}\\
&\Rightarrow \nabla\cdot(v^{\parallel}\nabla v^{\perp} - v^{\perp}\nabla v^{\parallel}) + v^{\perp}\nabla^2 v^{\parallel}\\
&\quad - v^{\parallel}\frac{\partial p^{\perp}}{\partial y} - \omega u^{\perp}v^{\parallel} = -v^{\parallel}\\
&\Rightarrow \nabla\cdot(v^{\parallel}\nabla v^{\perp} - v^{\perp}\nabla v^{\parallel}) + v^{\perp}\frac{\partial p^{\parallel}}{\partial y} - v^{\parallel}\frac{\partial p^{\perp}}{\partial y}\\
&\quad + \omega(u^{\parallel}v^{\perp} - u^{\perp}v^{\parallel}) = -v^{\parallel},
\end{aligned} \tag{B13}$$

where Eq. (B2) has been used. The two terms containing pressure gradients can be further manipulated as follows:

$$\begin{aligned}
&v^{\perp}\frac{\partial p^{\parallel}}{\partial y} - v^{\parallel}\frac{\partial p^{\perp}}{\partial y}\\
&= \frac{\partial}{\partial y}(v^{\perp}p^{\parallel} - v^{\parallel}p^{\perp}) + p^{\parallel}\frac{\partial w^{\perp}}{\partial z} - p^{\perp}\frac{\partial w^{\parallel}}{\partial z}\\
&= \frac{\partial}{\partial y}(v^{\perp}p^{\parallel} - v^{\parallel}p^{\perp}) + \frac{\partial}{\partial z}(w^{\perp}p^{\parallel} - w^{\parallel}p^{\perp})\\
&\quad + w^{\parallel}\nabla^2 w^{\perp} - w^{\perp}\nabla^2 w^{\parallel}\\
&= \frac{\partial}{\partial y}(v^{\perp}p^{\parallel} - v^{\parallel}p^{\perp}) + \frac{\partial}{\partial z}(w^{\perp}p^{\parallel} - w^{\parallel}p^{\perp})\\
&\quad + \nabla\cdot(w^{\parallel}\nabla w^{\perp} - w^{\perp}\nabla w^{\parallel}),
\end{aligned} \tag{B14}$$

where Eqs. (B3), (B4), (B7), and (B8) have been used. Substituting these terms back to Eq. (B13), we get

$$\begin{aligned}
&\nabla\cdot(v^{\parallel}\nabla v^{\perp} - v^{\perp}\nabla v^{\parallel} + w^{\parallel}\nabla w^{\perp} - w^{\perp}\nabla w^{\parallel})\\
&\quad + \frac{\partial}{\partial y}(v^{\perp}p^{\parallel} - v^{\parallel}p^{\perp}) + \frac{\partial}{\partial z}(w^{\perp}p^{\parallel} - w^{\parallel}p^{\perp})\\
&\quad + \omega(u^{\parallel}v^{\perp} - u^{\perp}v^{\parallel}) = -v^{\parallel}.
\end{aligned} \tag{B15}$$

On integrating this equation over the unit sectional area D, the integral of the divergence term is zero, which can be proved using the divergence theorem as described above. The integral $\int_{-1}^{1}\partial(v^{\perp}p^{\parallel} - v^{\parallel}p^{\perp})/\partial y\,dy$ is zero by virtue of periodicity on $y = \pm 1$, while the integral $\int_{-h}^{h}\partial(w^{\perp}p^{\parallel} - w^{\parallel}p^{\perp})/\partial z\,dz$ is also zero by virtue of $w = 0$ on $z = \pm h$. It follows that, when averaged over D, Eq. (B15) yields

$$\bar{v}^{\parallel} = -\omega\overline{(u^{\parallel}v^{\perp} - u^{\perp}v^{\parallel})}. \tag{B16}$$

Finally, from Eqs. (B12) and (B16), we deduce that

$$\bar{u}^{\perp} = -\bar{v}^{\parallel} = \omega\overline{(u^{\parallel}v^{\perp} - u^{\perp}v^{\parallel})}. \tag{B17}$$

This serves to prove that the secondary flow rate is the same when the pressure gradient is applied in a direction parallel or normal to the stripes.

[1] T. V. Nizkaya, E. S. Asmolov, and O. I. Vinogradova, Phys. Rev. E **90**, 043017 (2014).
[2] C. L. M. H. Navier, Mém. Acad. R. Sci. Inst. France **6**, 389 (1823).
[3] E. Lauga and H. A. Stone, J. Fluid Mech. **489**, 55 (2003).
[4] C. Ybert, C. Barentin, C. Cottin-Bizonne, P. Joseph, and L. Bocquet, Phys. Fluids **19**, 123601 (2007).
[5] T. Lee, E. Charrault, and C. Neto, Adv. Colloid Interface Sci. **210**, 21 (2014).
[6] J. R. Philip, ZAMP **23**, 353 (1972).
[7] A. V. Belyaev and O. I. Vinogradova, J. Fluid Mech. **652**, 489 (2010).
[8] E. S. Asmolov, J. Zhou, F. Schmid, and O. I. Vinogradova, Phys. Rev. E **88**, 023004 (2013).
[9] S. Chakraborty, *Microfluidics and Microscale Transport Processes* (CRC Press, Boca Raton, 2013).
[10] C. Y. Wang, Chem. Eng. Comm. **200**, 587 (2013).
[11] G. C. Shit, A. Mondal, A. Sinha, and P. K. Kundu, Colloids Surf. A **489**, 249 (2016).
[12] C. O. Ng, Mech. Res. Comm. **76**, 57 (2016).
[13] O. I. Vinogradova, Langmuir **11**, 2213 (1995).
[14] C. O. Ng and C. Qi, Proc. R. Soc. A **471**, 20150200 (2015).
[15] J. Pedlosky, *Geophysical Fluid Dynamics* (Springer-Verlag, New York, 1987).
[16] V. Vidyanidhu and S. D. Nigam, J. Math. Phys. Sci. **1**, 85 (1967).
[17] K. Kamrin, M. Z. Bazant, and H. A. Stone, J. Fluid Mech. **658**, 409 (2010).